CrossMark

Discovery of a Collimated Jet from the Low-luminosity Protostar IRAS 16253−2429 in a Quiescent Accretion Phase with the JWST

Mayank Narang[1,2] , P. Manoj[2] , Himanshu Tyagi[2] , Dan M. Watson[3] , S. Thomas Megeath[4] , Samuel Federman[4] ,
Adam E. Rubinstein[3] , Robert Gutermuth[5] , Alessio Caratti o Garatti[6] , Henrik Beuther[7] , Tyler L. Bourke[8] ,
Ewine F. Van Dishoeck[9,10] , Neal J. Evans, II[11] , Guillem Anglada[12] , Mayra Osorio[12] , Thomas Stanke[10] ,
James Muzerolle[13] , Leslie W. Looney[14,15] , Yao-Lun Yang[16] , Pamela Klaassen[17] , Nicole Karnath[18,19] ,
Prabhani Atnagulov[20] , Nashanty Brunken[9] , William J. Fischer[13] , Elise Furlan[21] , Joel Green[13] , Nolan Habel[22] ,
Lee Hartmann[23] , Hendrik Linz[7,24] , Pooneh Nazari[9] , Riwaj Pokhrel[25] , Rohan Rahatgaonkar[26] , Will R. M. Rocha[27] ,
Patrick Sheehan[15] , Katerina Slavicinska[9] , Amelia M. Stutz[28] , John J. Tobin[15] , Lukasz Tychoniec[29] , and Scott Wolk[19]

[1] Academia Sinica Institute of Astronomy & Astrophysics, 11F of Astro-Math Bldg., No.1, Sec. 4, Roosevelt Road, Taipei 10617, Taiwan
[2] Department of Astronomy and Astrophysics Tata Institute of Fundamental Research Homi Bhabha Road, Colaba, Mumbai 400005, India
[3] University of Rochester, Rochester, NY, USA
[4] University of Toledo, Toledo, OH, USA
[5] University of Massachusetts Amherst, Amherst, MA, USA
[6] INAF-Osservatorio Astronomico di Capodimonte, IT, Italy
[7] Max Planck Institute for Astronomy, Heidelberg, Baden Wuerttemberg, DE, Germany
[8] SKA Observatory, Jodrell Bank, Lower Withington, Macclesfield SK11 9FT, UK
[9] Leiden Observatory, Universiteit Leiden, Leiden, Zuid-Holland, The Netherlands
[10] Max-Planck Institut für Extraterrestrische Physik, Garching bei München, DE, Germany
[11] Department of Astronomy, The University of Texas at Austin, 2515 Speedway, Stop C1400, Austin, Texas 78712-1205, USA
[12] Instituto de Astrofísica de Andalucía, CSIC, Glorieta de la Astronomía s/n, E-18008 Granada, ES, Spain
[13] Space Telescope Science Institute, 3700 San Martin Drive, Baltimore, MD 21218, USA
[14] Department of Astronomy, University of Illinois, 1002 West Green Street, Urbana, IL 61801, USA
[15] National Radio Astronomy Observatory, 520 Edgemont Road, Charlottesville, VA 22903 USA
[16] Star and Planet Formation Laboratory, RIKEN Cluster for Pioneering Research, Wako, Saitama 351-0198, Japan
[17] United Kingdom Astronomy Technology Centre, Edinburgh, GB, UK
[18] Update to Space Telescope Science Institute, 3700 San Martin Drive, Baltimore, MD 21218, USA
[19] Center for Astrophysics Harvard & Smithsonian, Cambridge, MA, USA
[20] Ritter Astrophysical Research Center, Dept. of Physics and Astronomy, University of Toledo, Toledo, OH, USA
[21] Caltech/IPAC, Pasadena, CA, USA
[22] Jet Propulsion Laboratory, Pasadena, CA, USA
[23] University of Michigan, Ann Arbor, MI, USA
[24] Friedrich-Schiller-Universität, Jena, Thüringen, DE, Germany
[25] Ritter Astrophysical Research Center, Dept. of Physics and Astronomy, University of Toledo, Toledo, OH, 43606, USA
[26] Gemini South Observatory, La Serena, CL, USA
[27] Laboratory for Astrophysics, Leiden Observatory, Universiteit Leiden, Leiden, Zuid-Holland, The Netherlands
[28] Departamento de Astronomía, Universidad de Concepción,Casilla 160-C, Concepción, Chile
[29] European Southern Observatory, Garching bei München, DE, Germany

Abstract

Investigating Protostellar Accretion (IPA) is a JWST Cycle 1 GO program that uses NIRSpec integral field units and MIRI Medium Resolution Spectrograph to obtain 2.9–28 μm spectral cubes of young, deeply embedded protostars with luminosities of 0.2–10,000 $L_\odot$ and central masses of 0.15–12 $M_\odot$. In this Letter, we report the discovery of a highly collimated atomic jet from the Class 0 protostar IRAS 16253−2429, the lowest-luminosity source ($L_{\rm bol} = 0.2\,L_\odot$) in the IPA program. The collimated jet is detected in multiple [Fe II] lines and [Ne II], [Ni II], and H I lines but not in molecular emission. The atomic jet has a velocity of about $169 \pm 15\,{\rm km\,s^{-1}}$, after correcting for inclination. The width of the jet increases with distance from the central protostar from 23 to 60 au, corresponding to an opening angle of $2°\!.6 \pm 0°\!.5$. By comparing the measured flux ratios of various fine-structure lines to those predicted by simple shock models, we derive a shock speed of $54\,{\rm km\,s^{-1}}$ and a preshock density of $2.0 \times 10^3\,{\rm cm^{-3}}$ at the base of the jet. From these quantities and using a suite of jet models and extinction laws, we compute a mass-loss rate between 0.4 and $1.1 \times 10^{-10}\,M_\odot\,{\rm yr^{-1}}$. The low mass-loss rate is consistent with simultaneous measurements of low mass accretion rate ($2.4 \pm 0.8 \times 10^{-9}\,M_\odot\,{\rm yr^{-1}}$) for IRAS 16253−2429 from JWST observations, indicating that the protostar is in a quiescent accretion phase. Our results demonstrate that very low-mass protostars can drive highly collimated, atomic jets, even during the quiescent phase.

Unified Astronomy Thesaurus concepts: Protostars (1302); Jets (870); Stellar jets (1607); Stellar winds (1636); Stellar accretion (1578); Accretion (14)

1. Introduction

Jets and outflows from protostars and pre-main-sequence stars play a crucial role in the process of star formation. These

dynamic phenomena are instrumental in facilitating the removal of angular momentum from the surrounding disk material, thereby enabling efficient accretion of mass onto the central object (e.g., Pudritz et al. 2007; Shang et al. 2007; Frank et al. 2014; Bally 2016; Hartmann et al. 2016; Ray & Ferreira 2021). Accretion-driven outflows/jets also play vital roles in shaping the initial mass function (IMF; e.g., Guszejnov et al. 2022; Lebreuilly et al. 2023) and can inject energy and momentum into the surroundings and disperse a significant fraction of the protostellar envelope, which limits star formation efficiency (e.g., Fall et al. 2010; Frank et al. 2014; Federrath 2015; Habel et al. 2021; Pokhrel et al. 2021; Appel et al. 2023; Hsieh et al. 2023).

Despite their unquestionable significance, the precise origins of protostellar jets and outflows remain uncertain and continue to be a subject of debate. Among the various proposed mechanisms, the most widely accepted one is magnetocentrifugal acceleration (Blandford & Payne 1982; Pudritz & Norman 1983; Pelletier & Pudritz 1992; Wardle & Koenigl 1993; Najita & Shu 1994; Shu et al. 1994; Matt & Pudritz 2005, 2008; Frank et al. 2014). According to this model, material situated near the surface of the inner parts of the disk is ejected centrifugally along the rotating magnetic field lines. As the outflow progresses beyond the Alfvén surface where the kinetic energy matches the magnetic energy, the dynamics begin to dominate over the magnetic field, resulting in a predominantly toroidal magnetic configuration. The tension force generated by these magnetic loops focuses the outflowing material into a narrow jet along the rotational axis of the circumstellar disk that originally launched the (MHD) wind (Blandford & Payne 1982; Spruit 1996; Ray & Ferreira 2021). As a result, highly collimated bipolar jets are formed.

Infrared emission lines of [Fe II] and H_2 are well-known tracers of shocked gas and have been used to trace jets and outflows from protostars (e.g., Caratti o Garatti et al. 2006; Agra-Amboage et al. 2014; Bally 2016; Watson et al. 2016; Reipurth et al. 2019; Yang et al. 2022; Beuther et al. 2023; Harsono et al. 2023; Ray et al. 2023; Rubinstein et al. 2023). These lines serve as excellent diagnostics for deriving the physical conditions of the collimated jets as well as the shocked molecular gas in the outflow (Ray et al. 2023). Harnessing the spatial and spectral resolution as well as the sensitivity of JWST, we can gain a deeper understanding of the launching of and feedback from the protostellar jets/outflows.

Investigating Protostellar Accretion (IPA) across the mass spectrum is a JWST Cycle 1 medium GO program (Program ID 1802, PI: Tom Megeath; Megeath et al. 2021; Federman et al. 2023a; Rubinstein et al. 2023; D. Watson et al. 2024, in preparation; Nazari et al. 2024). The IPA program aims to study the processes that drive protostellar accretion and accretion-driven jets/outflows as a function of protostellar mass. The IPA protostellar sample consists of five sources that range in bolometric luminosities from 0.2 to 10,000 $L_\odot$ and in central masses from 0.15 to 12 $M_\odot$. These protostars are in the Class 0 phase, during which most of the stellar mass is accreted (e.g., Fischer et al. 2017; Federman et al. 2023b; Narang et al. 2023).

The protostar IRAS 16253−2429 is the lowest-luminosity source in the IPA sample. It is located in a relatively isolated region of the Ophiuchus molecular cloud (Khanzadyan et al. 2004; Stanke et al. 2006; Barsony et al. 2010). The protostar

has a bolometric luminosity of only 0.2 $L_\odot$ and a bolometric temperature of 42 K (R. Pokhrel et al. 2024, in preparation; also see Pokhrel et al. 2023) and an internal luminosity below 0.15 $L_\odot$ (R. Pokhrel et al. 2024, in preparation). Being only at a distance of 140 pc (average of ρ-Ophiuchi molecular cloud members; Zucker et al. 2020) and relatively isolated, IRAS 16253−2429 is an ideal target to study the morphology and kinematics of jets from very low-mass (<0.2 $M_\odot$) protostars (Yen et al. 2017; Aso et al. 2023).

Extensive studies have been conducted on this protostar, particularly at (sub)millimeter wavelengths (Stanke et al. 2006; Tobin et al. 2011; Yen et al. 2017; Hsieh et al. 2019). These observations have revealed the presence of a central protostar associated with a bipolar outflow identified in CO, as well as a Keplerian disk. However, no collimated molecular jet in the low-J lines of CO or SiO has been detected from the system (Aso et al. 2023). This is consistent with the low detection rate of molecular jets from low-luminosity protostars (e.g., Podio et al. 2021). Recent observations with ALMA have estimated the dynamical mass of the central source to be between 0.12 and 0.17 $M_\odot$ (Aso et al. 2023), indicating that IRAS 16253 −2429 has already accreted a mass above the hydrogen-burning limit. The protostar also has a dust disk with a diameter of 15 au (Aso et al. 2023) with a mass of $2 \times 10^{-3} M_\odot$. The envelope mass of IRAS 16253−2429 has been estimated from (sub)millimeter observations to be in the range of 0.2–1 $M_\odot$ (within a radius of ∼4200 au; Stanke et al. 2006; Enoch et al. 2008; Tobin et al. 2011). The disk-to-envelope mass ratio for IRAS 16253−2429, therefore, is ≪0.01 and is consistent with the values reported for Class 0 protostars by Federman et al. (2023).

Figure 1 shows the Spitzer Infrared Array Camera (IRAC) images of the IRAS 16253−2429 field, which reveal a bipolar hourglass structure in the northeast to southwest direction. This distinctive shape is traced by the outflow cavities in H_2 and the continuum. The bipolar outflow from the source extends up to 2′ in size, corresponding to a physical scale of 16800 au or 0.08 pc. In addition to the imaging, the Spitzer Infrared Spectrograph (IRS) instrument also carried out spectral scan mapping of the protostar (Barsony et al. 2010). The Spitzer IRS spectra detected six pure rotational H_2 (0-0 S(2) to 0-0 S(7)) lines along the protostellar outflow. However, no fine-structure (FS) lines were detected from the protostar with Spitzer/IRS.

2. Observations and Data Reduction

Our primary objective with the JWST observations was to perform spectral imaging by combining the integral field unit (IFU) observations from the Mid-Infrared Instrument (MIRI) Medium Resolution Spectrograph (MRS; Rieke et al. 2015; Wright et al. 2015) and the Near Infrared Spectrograph (NIRSpec; Böker et al. 2022; Jakobsen et al. 2022) covering 2.87–28 μm. The NIRSpec IFU and MIRI MRS observations were conducted nearly simultaneously. The details of the observation log are provided in Table 1.

For the NIRSpec IFU observations, we utilized the F290L/ G395M filter/grating combination, which has a wavelength coverage from 2.87 to 5.10 μm and a nominal resolving power of ∼1000.[30] To ensure comprehensive coverage of the protostellar jet/outflow, we employed a 2×2 mosaic pattern
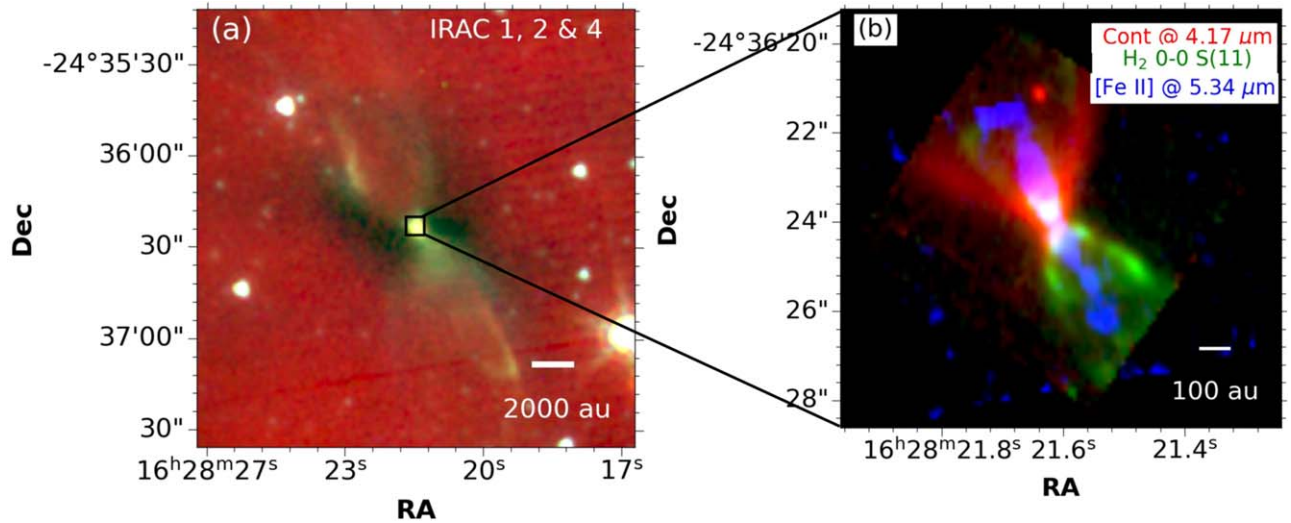

Figure 1. (a) The Spitzer IRAC three-color (IRAC 3.6, 4.5, and 8 μm are red, green, and blue, respectively) image of the IRAS 16253−2429 field. The field of view is $2' \times 2'$. The black square in the center represents a $6'' \times 6''$ field centered on the JWST observations. (b) A zoomed-in view of the NIRSpec and MIRI channel 1 short (A) field with the red representing continuum emission at 4.17 μm, the green showing H$_2$ 0-0 S(11) at 4.18 μm, and the blue depicting [Fe II] at 5.34 μm. A local continuum has been subtracted to make the line maps.

Table 1
The Log of the JWST Observations (Program ID 1802) Presented in This Paper

Obs.	Obs. No.	R.A.	Decl.	Hours	Start (UT)	End (UT)
NIRSpec IFU IRAS 16253−2429	015	16 28 21.62[a]	−24 36 24.16[a]	3.43	2022 Jul 22 15:09:15	2022 Jul 22 17:59:43
MIRI MRS IRAS 16253−2429	013	16 28 21.62[a]	−24 36 24.16[a]	7.43	2022 Jul 23 04:04:41	2022 Jul 23 09:58:57
MIRI MRS IRAS 16253−2429 background	014	16 28 27.756	−24 37 46.95	1.86	2022 Jul 23 10:02:33	2022 Jul 23 11:35:19

Note.
[a] The coordinates are the field center of the 2×2 mosaics.

with a 10% overlap and a four-point dither mode. The NIRSpec mosaic covers $\sim 6'' \times 6''$ field centered at R.A. = $16^h28^m21\overset{s}{.}62$ and decl. = $-24^d36^m24\overset{s}{.}16$. The total exposure time, which accounted for overheads, amounted to 3.43 hr (for further detail, see Federman et al. 2023). Using the background star in the NIRSpec field of IRAS 16253-2429, Federman et al. (2023) measured the NIRSpec FWHM to be between 0″19 and 0″20.

IRAS 16253−2429 was observed using all four channels of the MIRI MRS with wavelength coverage from 4.9 to 27.9 μm, with a spectral resolving power ranging from $\sim$1500 to 4000 (Jones et al. 2023).[31] The spatial resolution of MIRI MRS ranges from $\sim$0″27 to 1″ (Law et al. 2023). Similar to the NIRSpec observations, we employed a 2×2 mosaic pattern with a 10% overlap and a four-point dither for the MIRI observations. The total exposure time, including overheads, for the science target amounted to 7.43 hr. Additionally, a dedicated background observation with a similar setup and an exposure time of 1.86 hr (including overheads) was obtained. The dedicated background field was positioned approximately 118″ away from the target. The spatial coverage for MIRI varies from channel to channel with channel 1 short covering $\sim 6'' \times 6''$, while for channel 4 long the coverage is $\sim 15'' \times 15''$. The orientation and the field coverage of the MIRI MRS instrument are also different from the NIRSpec IFU.[32] In addition, MIRI

parallel imaging observations were obtained at both MIRI pointings.

We reduced the NIRSpec IFU using the JWST pipeline version 1.9.5 and the JWST Calibration References Data System context version jwst_1069.pmap. Our analysis of the NIRSpec data showed the presence of several hot pixels that were being missed by the JWST outlier detection step. As these hot pixels were a function of wavelength and time, a universal dark mask could not be used. To remedy this, we used a custom outlier detection algorithm for the NIRSpec observations to remove the hot pixels (see Federman et al. 2023).

To reduce the MIRI data, we used the JWST pipeline version 1.11.3 and the JWST Calibration References Data System context version jwst_1100.pmap. We used the standard Stage-1 JWST pipeline *Detector1Pipeline* to reduce the MIRI MRS data starting from *uncal* data. In Stage-2 (*Spec2Pipeline*), the dedicated background was subtracted, and the residual fringe correction was also performed. The Stage-3 *Spec3Pipeline* step was then run with the *CubeBuildStep* set to "band" mode such that each channel and each band are reduced as a separate fits file. However, on examining the dedicated background IFU image, we detected emission from the H$_2$ S (1) (17.035 μm) and H$_2$ S(2) (12.279 μm) molecular lines. Therefore we also reduced the MIRI MRS data without subtracting the dedicated background. We have used these non-background subtracted data cubes for measuring the extinction in Section 3.3.

During our analysis of the data obtained from the MIRI MRS and NIRSpec IFU instruments, we found a positional offset

---

[31] Also see https://jwst-docs.stsci.edu/jwst-mid-infrared-instrument/miri-observing-modes/miri-medium-resolution-spectroscopy.
[32] https://jwst-docs.stsci.edu/jwst-observatory-characteristics/jwst-position-angles-ranges-and-offsets

Table 2
The Ionic and Atomic Lines Reported in This Work

Wavelength (μm)	Species and Transition		A_{ul} (s^{-1})	E_{up} (K)	References
	Upper State—Lower State				
4.052	H I (Brα)	$n = 5 - 4$	2.69×10^{6}	151492	(2)
4.115	[Fe II]	$^{4}F_{7/2} - ^{6}D_{9/2}$	7.71×10^{-6}	3496	(1,2)
4.889	[Fe II]	$^{4}F_{7/2} - ^{6}D_{7/2}$	9.3×10^{-5}	3496	(2)
5.340	[Fe II]	$^{4}F_{9/2} - ^{6}D_{9/2}$	2.37×10^{-5}	2694	(1,2)
12.814	[Ne II]	$^{2}P_{1/2} - ^{2}P_{3/2}$	8.32×10^{-3}	1123	(2)
17.936	[Fe II]	$^{4}F_{7/2} - ^{4}F_{9/2}$	5.84×10^{-3}	3496	(2)
24.519	[Fe II]	$^{4}F_{5/2} - ^{4}F_{7/2}$	3.93×10^{-3}	4083	(2)
25.249	[S I]	$^{3}P_{1} - ^{3}P_{2}$	1.4×10^{-3}	570	(2)
25.988	[Fe II]	$^{6}D_{7/2} - ^{6}D_{9/2}$	2.14×10^{-3}	554	(1,2)

References. (1) Tayal & Zatsarinny 2018; (2) Kramida et al. 2023.

between the two instruments. To accurately determine and quantify the offset between the two instruments, we compared the overlapping wavelength regions of MIRI MRS channel 1 short and the NIRSpec IFU cubes. The positional offset between these two instruments (MIRI−NIRSpec) was ΔR. A. = 0″37 and Δdecl. = 0″67. We further refined the position of the MIRI MRS field by aligning it with Spitzer and Gaia data of the stellar sources detected in the MIRI parallel image. We then adjusted the NIRSpec position using the determined offset between it and the MRS. We use these refined positions in our analysis. For further elaboration and in-depth information concerning this positional offset, see Federman et al. (2023).

3. Jets from IRAS 16253-2429

3.1. Morphology

The JWST observations of IRAS 16253-2429 with the NIRSpec IFU and MIRI MRS instruments reveal atomic jets, molecular outflows, and envelope cavity structures at spatial scales down to 30 au. In Figure 1, we present a comparison between the Spitzer IRAC (IRAC 3.6, 4.5, and 8 μm; Figure 1(a)) observations of the protostar, covering a field of view of $2' \times 2'$, and the NIRSpec IFU + MIRI MRS observations (Figure 1(b)) focused within the inner 6″ (also see Federman et al. 2023). Figure 1(a) shows the full spatial extent of the protostellar outflow from IRAS 16253−2429 as seen by Spitzer. The black rectangle shows the field of view of the JWST observations. Figure 1(b) shows the zoomed-in inner ∼6″ region of the protostar as observed with JWST. The 4.17 μm continuum emission is primarily due to the scattered light from the central source and is shown in red; it traces the extent of the outflow cavity carved out of the envelope. The molecular outflow traced by H$_2$ 0-0 S(11) emission at 4.18 μm is shown in green. The atomic jet seen in the [Fe II] line at 5.34 μm is shown in blue. The JWST observations show that IRAS 16253−2429 exhibits the distinctive "wasp-waist" shape (Barsony et al. 2010), even within the inner 6″ region surrounding the protostar. Figure 1(b) further shows that the scattered light cavity is much broader than the molecular emission from H$_2$ (also see Federman et al. 2023 and M. Narang et al. 2024, in preparation).

The wavelength range covered by the MIRI MRS and NIRSpec IFU instruments encompasses several atomic and FS lines, including multiple lines of [Fe II]. In Table 2, we have listed the bright atomic and ionic lines detected toward IRAS

16253-2429, along with their wavelength, Einstein A coefficient A_{ul}, and upper state energy E_{up}.

In Figure 2, we present the line maps of all the detected [Fe II] lines observed toward IRAS 16253−2429. These [Fe II] lines trace a highly collimated jet originating from the central protostar. This is the first time (at any wavelength) that a collimated jet has been detected from IRAS 16253−2429. The jet appears brighter on the northern side and weaker to the south; this is due to the relatively higher line-of-sight extinction toward the southern cavity (see Section 3.4).

We further find that there are knots at both ends of the jet (see Figure 2) at around 400 au from the central protostar (see also Federman et al. 2023). The southern knot is best detected in the [Fe II] line at 5.34 μm, with a tentative detection in the [Fe II] lines at 17.936 and 25.988 μm. The northern knot is clearly seen in five of the six [Fe II] line maps presented in Figure 2 although it is not fully mapped in the 5.34 μm line and is only faintly seen in the 24.5 μm line. If we draw a line from the central protostar to the northern- and southernmost knots, we find that the jet seen in [Fe II] at 5.34 μm does not fall on this line. The northern knot is clearly offset to the east from the axis of the rest of the northern jet. We also find that the jet has a slight curvature, suggesting that it might be precessing (see also Barsony et al. 2010).

In Figure 3, we present maps of other atomic FS lines along with the Br-α line at 4.052 μm. We find that the FS lines of [Ne II] at 12.81 μm and the [Ni II] at 6.64 μm also trace the jet seen in [Fe II]. The [Ne II] jet also shows faint knots at both ends similar to the [Fe II] jets. The [S I] emission at 25.25 μm, however, is concentrated on the protostar and does not appear to trace the jet (see Figure 3). The Br-α line observed with NIRSpec appears to trace the jet and shows the knot on the northern side (see Figure 3). Interestingly, Br-α emission is stronger in the extended jets than at the central source. This suggests that the H I lines observed from protostars via spatially unresolved spectroscopy might have a large contribution from the jet component; the dominant jet component makes it difficult to isolate emission in this line from accretion flows (see Hartmann et al. 2016; Federman et al. 2023).

3.2. Jet Width

Given the high signal-to-noise and high angular resolution at 5.34 μm (0″28; Law et al. 2023), it is possible to measure the width of the jet as a function of distance from the protostar. The jet has a position angle of 23° (measured from north toward east). We started by taking slices aligned perpendicular to the
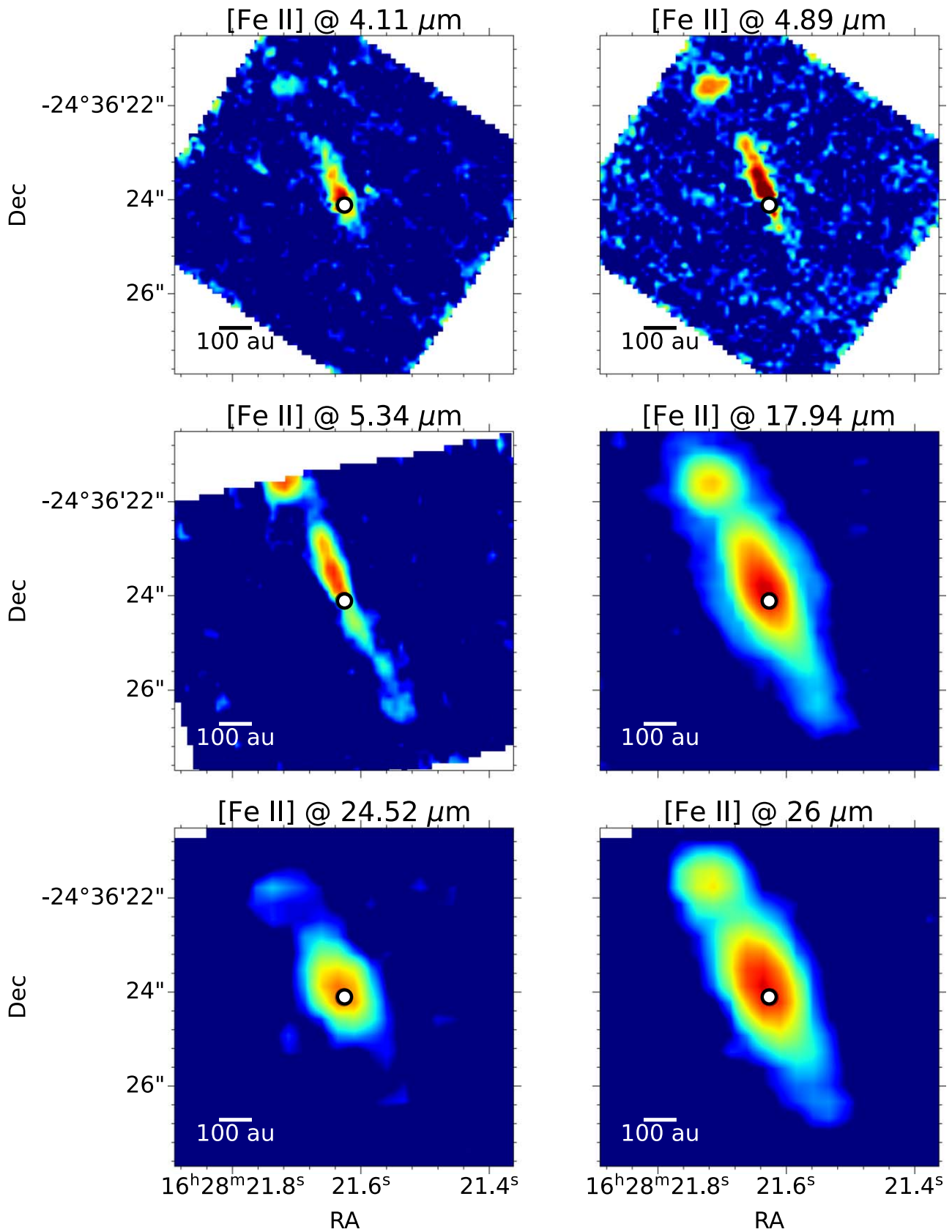
Figure 2. The morphology of [Fe II] lines detected toward IRAS 16253−2429. All these lines trace the collimated jet launched from the protostar. All images are shown on the same spatial scale. The white solid circle is the MIRI MRS 14 μm continuum position. The scale bar corresponding to 100 au is shown in the bottom left corner.
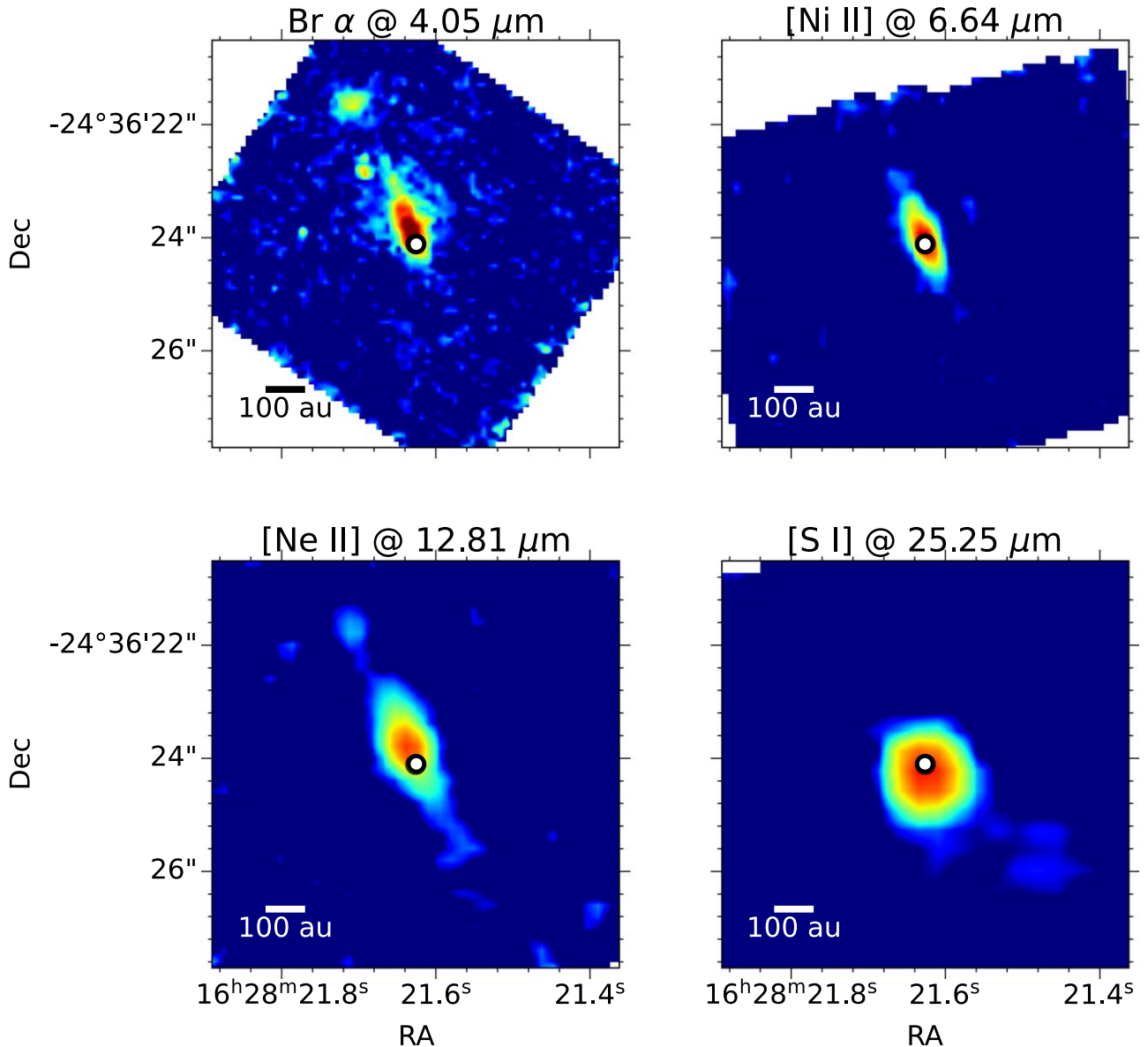
Figure 3. Morphology of the Br-α line and the other atomic FS lines detected toward IRAS 16253−2429. All images are shown on the same spatial scale. The white solid circle is the MIRI MRS 14 μm continuum position. The scale bar corresponding to 100 au is shown in the bottom left corner.

jet and averaged them over 3 pixel lengths along the jet as shown in Figure 4(a). We then fit the jet cross section in each of these averaged slices with a Gaussian, and the FWHM of the Gaussian is taken as the width of the jet in that slice.

In Figure 4(b) we show the width of the jet (FWHM) as a function of distance from the protostar. As can be seen from Figure 4(b), the jet appears to expand as we move away from the central protostar. We measure the FWHM of the slices adjacent to the protostar on either side and find the width of the jet close to the central protostar to be $0''.33 \pm 0''03$. This is comparable to the average point-spread function (PSF) FWHM of the MIRI MRS at 5.34 μm of $0''28$ (Law et al. 2023).

In Figure 4(c) we show the deconvolved jet widths (obtained by subtracting out the MIRI MRS point-spread function FWHM in quadrature) as a function of distance from the central protostar. From a linear fit to the jet width as a function of distance from the central protostar, we obtain the opening angle Θ (=slope /2)—the half angle subtended by the jet width at the launch point—as well as the jet width at the central

position (zero intercept). The average slope of the fit is 0.09 ± 0.02, corresponding to an opening angle of $2°6 \pm 0°5$. The jet width extrapolated to the source position is 23 ± 4 au, which we take as an upper limit for the jet width at the source location. Federman et al. (2023) used the NIRSpec observation of the [Fe II] line at 4.88 μm to measure the width of the jet from IRAS 16253−2429 at its brightest position and found a deconvolved jet width of $0''144$, which corresponds to 20.2 au.

3.3. Velocity Structure in the Jet

In order to explore the velocity structures within the jet, we first constructed a moment 1 map of the [Fe II] line at 5.34 μm as shown in Figure 5. The moment 1 map gives us the intensity-weighted velocity and is an excellent diagnostic tool for understanding the kinematic structures within the jets. As can be seen from Figure 5, the northern part of the jet is blueshifted with respect to the average velocity, while the southern jet is redshifted. We note that the velocity of the jet on
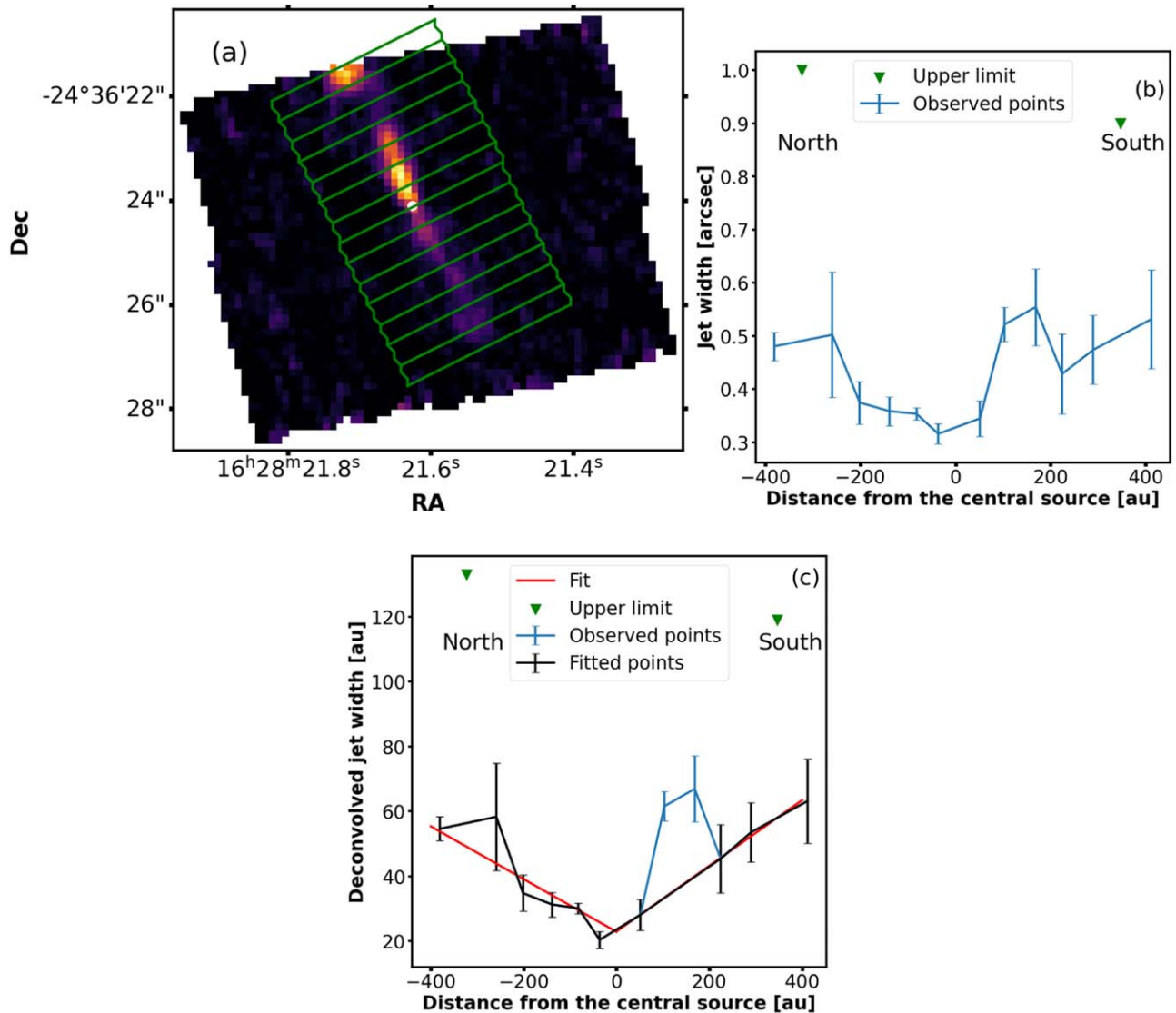
Figure 4. (a) The horizontal slices in green overlaid on top of the jet traced in [Fe II] at 5.34 μm mark slices that are 3 pixels wide along the jet direction. The jet width is computed from each of these green slices (see Section 3.2). The white circle represents the protostellar position. (b) The width (FWHM) of the jet as a function of distance from the central protostar. The negative distance corresponds to the northern jet, and the positive distance corresponds to the southern counterjet. (c) The deconvolved width (FWHM) of the jet as a function of distance from the central protostar. The fit to the jet width as a function of distance is shown as the red solid line. The green triangles in sub-figures (b) and (c) show the upper limits to the width at those points.

both sides is fairly constant and the maximum blueshift and redshift velocity difference is $\sim$130 km s^{-1}. This is much larger than the systemic cloud velocity (assumed to be V_{LSR}) of $\sim$4 km s^{-1} (Aso et al. 2023).

To further investigate the velocity structure of the jet, we constructed a position−velocity (PV) diagram, specifically for the [Fe II] line at 5.34 μm. In order to capture the full range of velocities, we selected a rectangular region around the protostar that is both wide and long enough to encompass the entire jet. We show the PV diagram for the [Fe II] line at 5.34 μm in Figure 6. From the PV diagram, it is apparent that as we move away from the central protostar (the driving source of the jet), the velocities on either side of the jet remain more or less constant. This is similar to what we found with the moment 1 map of [Fe II] at 5.34 μm (see Figure 5) as well. However, within the inner region covering approximately 50 au, we witness rapid changes in velocity in part due to the blending of emission from the jet and counterjet.

We also constructed PV diagrams for the other [Fe II] lines that were detected in MIRI MRS. We only make PV diagrams of lines detected in MIRI because the NIRSpec IFU has a much lower spectral resolution of $\sim$300 km s^{-1}.[33] We computed the velocity of each slice of the spectral cube by converting the wavelength shift with respect to the lab wavelengths (Koo et al. 2016; Tayal & Zatsarinny 2018) to a velocity shift. In Figure 7, we show PV diagrams of all the [Fe II] lines that we have detected from IRAS 16253−2429. Initially, the PV diagrams of the various [Fe II] lines did not align since uncertainties in the wavelength calibration can introduce offsets as large as 40 km s^{-1}, even within a single channel (especially for wavelengths longwards of 17.7 μm, channel 3 long(C); Argyriou et al. 2023). In Figure 7 we align the velocities in the PV diagrams by setting the mean velocity of the jet seen in each line to zero. Figure 7 shows that the jets display
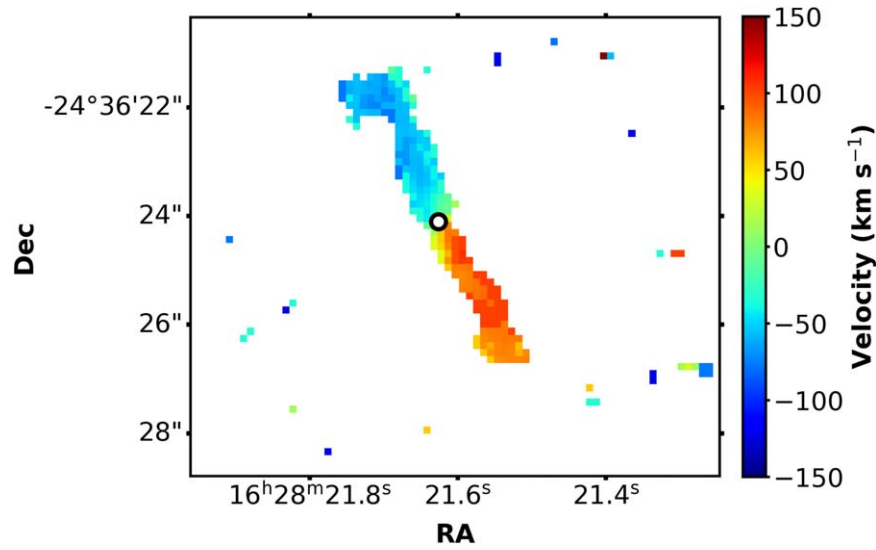
---

[33] https://jwst-docs.stsci.edu/jwst-near-infrared-spectrograph

Figure 5. The moment 1 map for the [Fe II] line at 5.34 μm. The white solid circle is the MIRI MRS 14 μm continuum position.
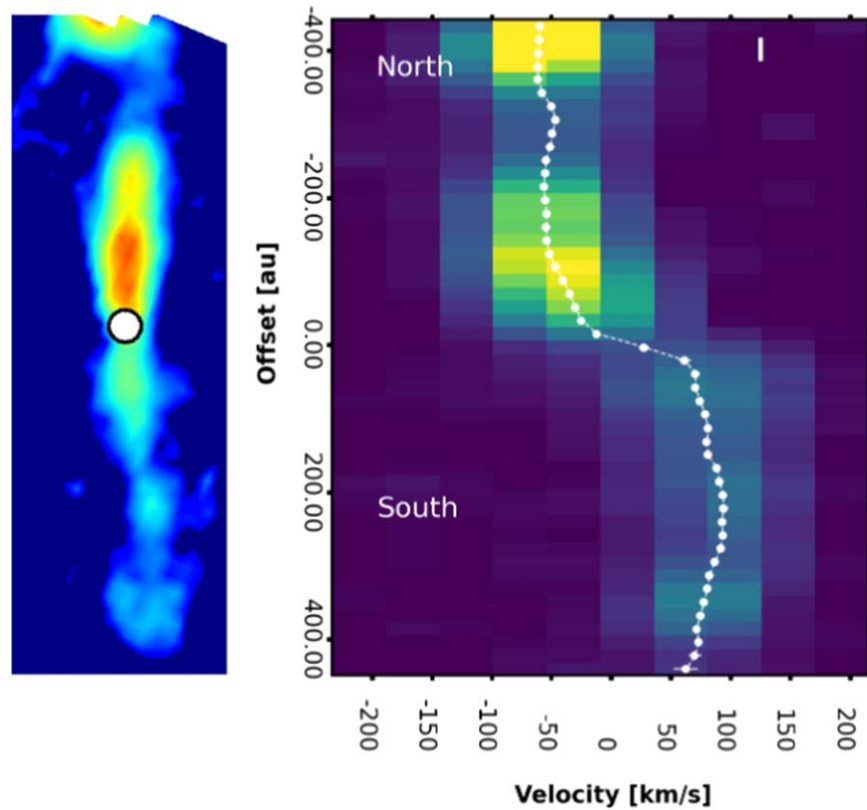

Figure 6. Left: image showing the line map of the [Fe II] line at 5.34 μm for comparison to the PV diagram. The width of the image gives the range over which we averaged the jet emission. The circle shows the 14 μm MIRI continuum position of the protostar. Right: the PV diagram for the [Fe II] line at 5.34 μm. The white circles represent the center of the Gaussian fit to the velocity channels, while the error bars represent the error in determining the center of the Gaussian fit. The white bar in the top left corner is the FWHM of the JWST MIRI PSF at 5.34 μm (0″28 or 39.2 au).

approximately symmetric velocities with respect to the central protostar. The difference in the peak positive and negative velocities for all the [Fe II] jets is similar, with an average value of $148 \pm 12 \, \mathrm{km \, s^{-1}}$. This consistency in peak jet velocities seen in different [Fe II] lines reinforces the notion of a coherent jet structure originating from the central protostar.

Using the PV diagrams we compute the line-of-sight jet velocity as half of the average peak-to-peak velocity. The average peak-to-peak velocity is $148 \pm 12 \, \mathrm{km \, s^{-1}}$, which gives

the line-of-sight jet velocity as $74 \pm 6 \, \mathrm{km \, s^{-1}}$. After correcting for the inclination of the jet using the measured inclination angle of $64°1 \pm 0°5$ from Aso et al. (2023), we obtain the velocity of the jet to be $169 \pm 15 \, \mathrm{km \, s^{-1}}$.

3.4. Measuring Extinction along the Jet

To derive the physical properties of the jet from the observed line maps, we first measure and quantify the line-of-sight
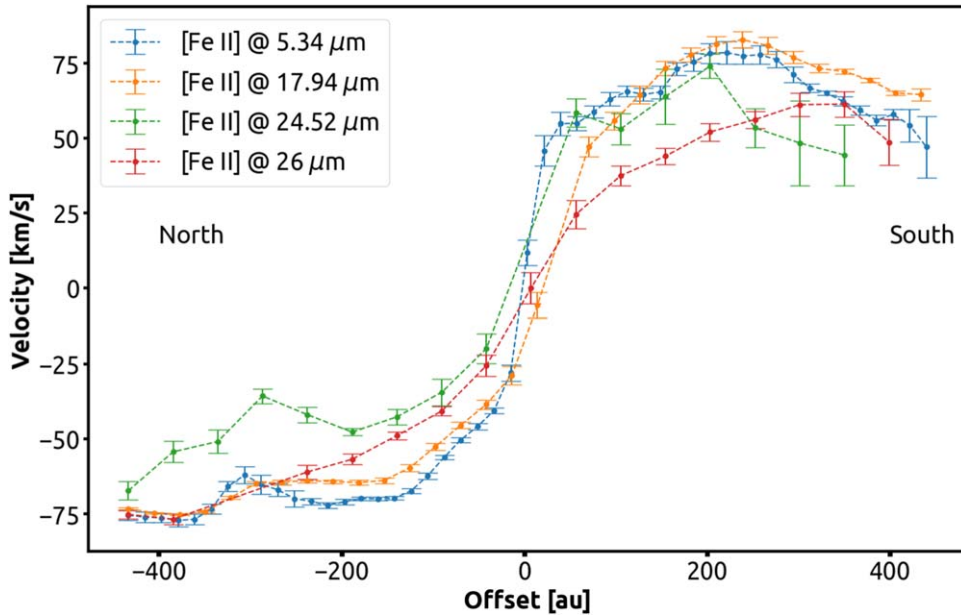
8

Figure 7. The PV diagrams of the [Fe II] lines detected in MIRI MRS aligned to a common average velocity.

extinction. To determine the spatially varying extinction toward IRAS $16253-2429$ outflow cavities, we used the molecular H_2 0-0 S(J) lines. Molecular H_2 lines have previously been used with Spitzer IRS to determine the extinction values (e.g., Barsony et al. 2010). Assuming that the H_2 is in local thermodynamical equilibrium (LTE) with an otho-para ratio of 3 we construct the rotation diagram for the H_2 lines (Figures 9 and 11).

In this diagram, the natural logarithm of the column density of H_2 molecules in the uth upper rotational state, N_u, divided by the degeneracy of that state g_u, $\ln(N_u/g_u)$, is plotted as a function of the upper state energy, E_u (energy of the uth rotational state; see, e.g., Maret et al. 2009; Neufeld et al. 2009; Barsony et al. 2010; Manoj et al. 2013). Here $g_u = g_{Ju} \times g_s$, with $g_{Ju} = 2Ju + 1$ and $g_s = 2s + 1$, where $s = 1$ for ortho-H_2 and $s = 0$ for para-H_2.

Assuming that H_2 emission is optically thin, then the number of H_2 molecules in the uth rotational state is given by

$$N_u = \frac{4 \pi F_{u,l} \lambda_{u,l}}{h c A_{u,l}}, \tag{1}$$

where h, c, $F_{u,l}$, $\lambda_{u,l}$, and $A_{u,l}$ are the Planck's constant, speed of light in vacuum, line flux within the aperture, wavelength, and Einstein A-coefficient, respectively, corresponding to the transition from the upper state u to the lower state l. We can compute an average rotational temperature T_{rot} for a relatively small range in E_u by fitting a straight line to the points in the observed rotational diagram. The negative of the inverse of the slope gives us the T_{rot}.

Under the LTE assumption, any deviation from this straight line in the narrow range of E_u is due to the extinction. By correcting for these deviations, we derive the line-of-sight extinction toward the protostars. To do so, we can simultaneously fit the rotation diagram and the correction for extinction. We restrict our analysis to H_2 lines between $6\mu m$ and $18\mu m$ (from H_2 0-0 S(1) to S(6)) to minimize non-LTE effects and also to avoid contamination from molecular gas phase CO (also see Rubinstein et al. 2023). In Table 3, we have

listed the wavelength, Einstein A coefficient A_{ul}, and upper state energy E_{up} of the H_2 transitions that are used to compute the line-of-sight extinction.

We used the extinction law from KP v05 Pontoppidan (2024, in preparation) presented in (Chapman et al. 2009) to derive the extinction toward the protostar (also see Section 3.5). We select apertures of radius $0\rlap{.}''8$ spaced $1\rlap{.}''1$ apart along the jet (see Figure 8 left) and measure the line fluxes within them. We then fit the extinction value A_V and two rotation temperatures simultaneously, one temperature representing cooler gas between H_2 0-0 S(1) and S(4) and the other slightly hotter gas between H_2 0-0 S(3) and S(6). In Figure 9 we show the H_2 rotation diagram for aperture 3 (centered on the protostar). Correcting for extinction, especially for the H_2 S(3) line (as it lies deep within the 10 μm silicate absorption feature), leads to an improved fit to the rotation diagram. Figure 11 in the Appendix shows the H_2 rotation diagrams for all apertures. The rotation temperature and A_V values for different apertures are listed in Table 4.

In Figure 8 (right), we show the variation of the line-of-sight extinction along the length of the jet. We find that the extinction rapidly rises as we move toward the protostar from north to south, reaching a maximum at the protostellar position, after which it remains relatively constant. A more detailed H_2 excitation analysis will be provided in a follow-up paper.

3.5. Physical Conditions along the Jet

We next investigated the physical conditions (shock speed and density) along the jet. We used the 1D shock and photoionization code MAPPINGS, version 5.1.18 (Sutherland et al. 2018), to model the shock. Furthermore, we used the [Fe II] collisional excitation network from (Tayal & Zatsarinny 2018) instead of the MAPPINGS-default database of atomic properties, CHIANTI (Del Zanna et al. 2021). Our shock models were computed for solar abundance (Asplund et al. 2009) with a frozen-in magnetic field $B = 15.8\ \mu G \times \sqrt{n/1000\ cm^{-3}}$. We implement the full magnetic
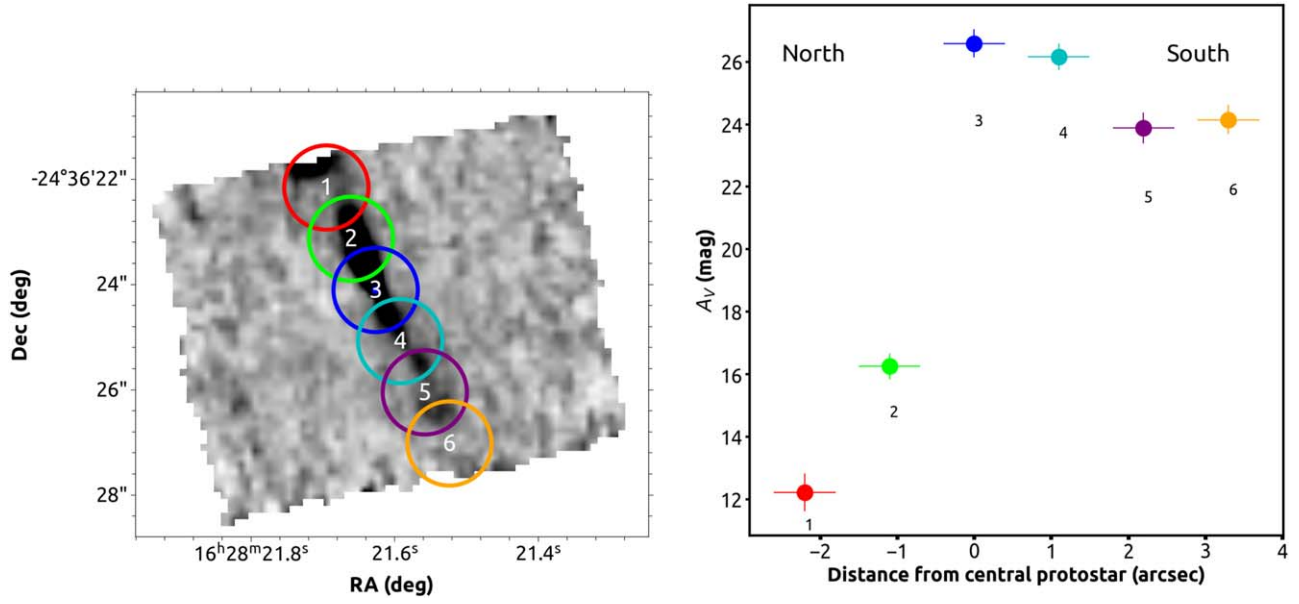
Figure 8. (left) The six apertures along the jet, where we measure the extinction and jet properties, overlaid on top of the [Fe II] jet at 5.34 μm shown in gray scale. The center of aperture 3 (blue circle) marks the position of the protostar. (right) The measured extinction value along in each of the aperture as a function of their position along the jet (from the northeast to southwest).

Table 3
The H$_2$ Lines Used to Estimate the Extinction along the Jet

Wavelength (μm)	Name	Upper State	Lower State	A_{ul} (s^{-1})	E_{up} (K)
17.035	H$_2$ 0-0 S(1)	$v = 0, J = (3)$	$v = 0, J = (1)$	4.758×10^{-10}	1015
12.279	H$_2$ 0-0 S(2)	$v = 0, J = (4)$	$v = 0, J = (2)$	2.753×10^{-9}	1681
9.665	H$_2$ 0-0 S(3)	$v = 0, J = (5)$	$v = 0, J = (3)$	9.826×10^{-9}	2503
8.025	H$_2$ 0-0 S(4)	$v = 0, J = (6)$	$v = 0, J = (4)$	2.641×10^{-8}	3474
6.910	H$_2$ 0-0 S(5)	$v = 0, J = (7)$	$v = 0, J = (5)$	5.872×10^{-8}	4586
6.109	H$_2$ 0-0 S(6)	$v = 0, J = (8)$	$v = 0, J = (6)$	1.140×10^{-7}	5830

Note. The wavelength, Einstein A-coefficient A_{ul}, and upper state energy are from Gordon et al. (2022).

and UV radiative precursor treatment by iterating and integrating the shock model to convergence.

We chose to use [Fe II] and [Ne II] as these lines have the largest extent in the jet. In Figure 10 we have plotted a nomogram for these lines from our the MAPPINGS shock model grid. The predicted ratio of [Ne II] at 12.81 μm and [Fe II] at 5.34 μm shown as blue lines runs along the y-axis and is sensitive to the shock speed (v_s), while the predicted ratio of [Fe II] lines at 17.93 and 5.34 μm shown as green lines (in Figure 10) that almost runs along the x-axis is sensitive to the pre-shock density (n_s). By placing the observed line ratios onto this nomogram, we can directly read off the shock speed and the pre-shock density.

The line fluxes along the jet were measured using the same aperture as in Figure 8 (left). The de-reddened flux ratios for the [Fe II] and [Ne II] lines were then placed onto the grid in Figure 10 as colored symbols (the color scheme for the apertures are the same as those in Figure 8 (left)), and the shock speed and pre-shock density were read off. We have listed the shock speed and pre-shock density derived for all the apertures in Table 4. Away from the central protostar, the pre-shock density rapidly falls, while the shock speed remains roughly constant.

The mass-loss rate from the protostar, $\dot{M}_{loss}$, can be expressed in terms of the pre-shock density, speed of the gas entering the shock, and jet radius as

$$\dot{M}_{loss} = \pi \times R^2 \times n_s v \times m_H, \qquad (2)$$

where R is the radius of the jet, ρ_s is the pre-shock density, v is the velocity of the gas entering the shock, and m_H is the mass of the hydrogen atom. We have already measured the jet velocity (v_{jet}) from the PV diagrams. Based on different jet models, the velocity of gas v used in Equation (2) can either be the bulk velocity of the jet as derived from the PV diagram ($v = v_{jet}$; e.g., pulsating jet models of Raga et al. 1990; Raga & Kofman 1992) or the sum of the shock speed and the jet velocity ($v = v_{jet} + v_s$ e.g., Rubinstein et al. 2023).

Using the pre-shock density and shock speed derived from the shock grid as well as the jet velocity derived from the PV diagram, and assuming that the jet has a cylindrical cross section with a radius equal to half the jet width measured at the location, we have computed the mass-loss rate along the jet from the protostar. The mass-loss rates for the various apertures are listed in Table 4. From all the models and

Table 4
The Outflow Properties for Each of the Apertures Shown in Figure 8

Aperture	Distance from Protostar (arcsec)	A_V	$T_{rot}1$ (K)	$T_{rot}2$ (K)	v_s (km s^{-1})	n_s (cm^{-3})	R (au)	$\dot{M}_{loss}$ for $v = v_{jet} + v_s$ ($M_\odot$ yr^{-1})	$\dot{M}_{loss}$ for $v = v_{jet}$ ($M_\odot$ yr^{-1})
1[a]	-2.2	12.3 ± 1.1	526 ± 35	797 ± 75	42	6×10^1	25.3 ± 5.1	1.5×10^{-11}	1.2×10^{-11}
2	-1.1	16.3 ± 0.7	585 ± 42	870 ± 88	51 ± 2	$2.4 ^{-0.8}_{+0.8} \times 10^2$	18.4 ± 3.6	$3.3 \pm 1.3 \times 10^{-11}$	$2.6 \pm 1 \times 10^{-11}$
3	0	26.6 ± 0.5	661 ± 74	849 ± 104	54 ± 1	$2 ^{+0.4}_{-0.3} \times 10^3$	11.5 ± 2	$1.1 \pm 0.3 \times 10^{-10}$	$8 \pm 2 \times 10^{-11}$
4	1.1	26.1 ± 0.6	685 ± 63	852 ± 101	52 ± 1	$3.2 ^{+0.4}_{-0.4} \times 10^2$	18.4 ± 3.6	$4.5 \pm 1 \times 10^{-11}$	$3.4 \pm 0.8 \times 10^{-11}$
5	2.2	23.9 ± 0.6	621 ± 54	840 ± 96	54 ± 1	$1 ^{+0.2}_{-0.3} \times 10^1$	25.3 ± 5.1	$2.7 \pm 0.9 \times 10^{-12}$	$2 \pm 0.7 \times 10^{-12}$
6	3.3	24.2 ± 0.7	672 ± 46	883 ± 101	52 ± 1	< 2	32.3 ± 6.6	$<8.6 \times 10^{-13}$	$<6.6 \times 10^{-13}$

Note. The extinction A_V, the rotation temperature of the H_2 Gas ($T_{rot}1$ and $T_{rot}2$), the shock speed, pre-shock densities, jet radius R (computed using the opening angle Θ and the jet width at the base) along with the mass-loss rate $\dot{M}_{loss}$ for each of the apertures shown in Figure 8. The errors associated with the mass-loss rate incorporate the uncertainties of the shock speed and pre-shock density, which are determined from the uncertainties in the line flux and the extinction A_V, the uncertainty in the measurement of the jet width, and that of the v_{jet} ($v_{jet} = 169 \pm 15$ km s^{-1}).
[a] In aperture 1, the northern knot is not entirely covered by the MIRI channel 1 FOV; therefore, the flux ratio might be overestimated.
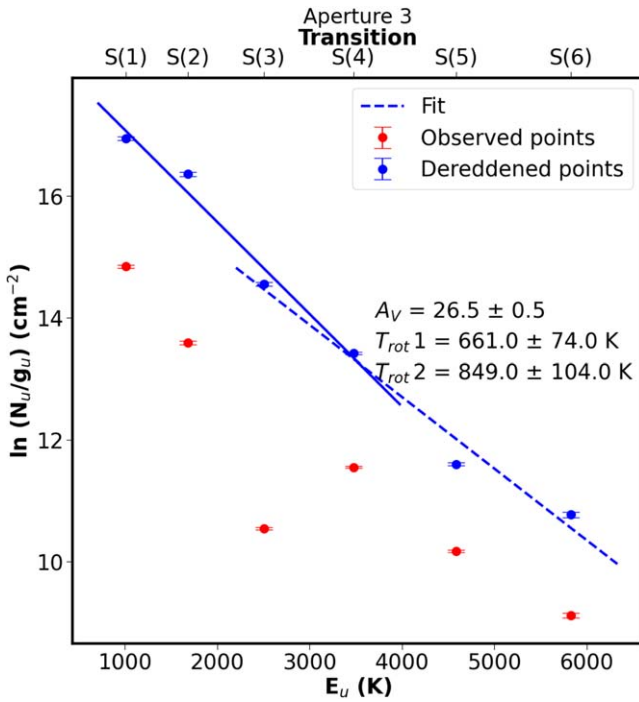

Figure 9. The H_2 rotation diagram for aperture 3 (centered on the protostar) from Figure 8. Also shown are the observed points (red), the de-reddened points (blue), and a fit to these points. The extinction value A_V as well as the rotation temperatures are listed in the figure. The y-error bars on the observed (red) points are computed based on the uncertainties in the integrated flux determined by a Gaussian fit to the lines using the measured uncertainties from the IFU error cubes. The y-error bars on the de-reddened (blue) points also incorporate the error in A_V from the fit.

positions, the highest mass-loss rate ($\dot{M}_{loss}$) from the protostar is $1.1 \pm 0.3 \times 10^{-10} M_\odot$ yr^{-1} .

In computing $\dot{M}_{loss}$ from the protostar, the largest uncertainty is not due to any measurement uncertainties but due to the uncertainty in the adopted extinction law. Chapman et al. (2009) have shown that the extinction law measured toward molecular clouds is highly variable and not only depends upon the molecular cloud but also the environment. To quantify the effects of using different extinction laws on our results, we repeated our analysis of computing extinction and estimating the mass-loss rate using two additional extinction laws, that of

McClure (2009) and Hensley & Draine (2021). We compute the mass-loss rate from the central protostar at the base of the jet (from aperture 3) assuming $v = v_{jet} + v_s$. We find that the mass-loss rate obtained using the extinction law from McClure (2009) is $5.3 \pm 1 \times 10^{-11} M_\odot$ yr^{-1} and using Hensley & Draine (2021) is $4.1 \pm 0.8 \times 10^{-11} M_\odot$ yr^{-1}. These $\dot{M}_{loss}$ values and the ones listed in Table 4 (for aperture 3) are within a factor of 3, indicating that the mass-loss rate of $\dot{M}_{loss}$ $1.1 \pm 0.3 \times 10^{-10} M_\odot$ yr^{-1} is robust.

4. Discussion

Our JWST observations reveal a highly collimated atomic jet in the IR FS lines and H I lines from the low-luminosity and very low-mass protostar IRAS 16253−2429. No collimated molecular jet is detected, and although IR H_2 emission is detected along the outflow cavity, it has a much wider opening angle and does not spatially follow the collimated atomic jet. The jet seen in the FS lines appears brighter on the blueshifted northeastern side that is facing us and is fainter to the southwest; this is due to the higher line-of-sight extinction toward the southwestern cavity (see Figure 8).

The jets on either side appear to have similar velocities that more or less remain constant as a function of distance from the driving source. The jet velocity, corrected for inclination effects (using the inclination of 64°.1), is 169 ± 15 km s^{-1}. The collimated jet seen in the JWST line images extends up to about 400 au (see Figure 7; 445 au after correcting for inclination) from the driving source on either side. This implies a dynamical timescale of ∼12.5 yr, suggesting that the jet seen in the JWST IFUs was ejected only in the last 12.5 yr.

The width of the jet (FWHM) at the base is marginally resolved and is ∼23 ± 4 au, and the jet tends to widen as it moves away from the central source with an opening angle $\Theta = 2°.6$. If the jet is ballistically confined, then the opening angle can be expressed as a ratio of the sound speed within the jet and the jet speed:

$$\Theta = \frac{c_s}{v_{jet}}, \quad (3)$$

where v_{jet} is the jet velocity of 169 ± 15 km s^{-1} and c_s is the sound speed (Ray & Ferreira 2021). If we assume that the shock temperature is 10,000 K (e.g., Ray & Ferreira 2021) then the sound speed $c_s = 10$ km s^{-1}, which gives an opening angle
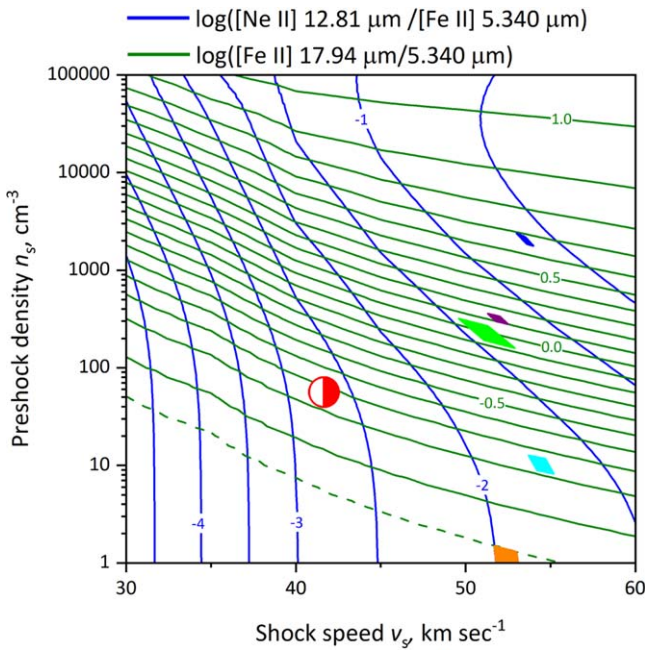
Figure 10. Nomogram from the MAPPINGS shock model grid showing the line ratios of three [Fe II] and [Ne II] lines. The ratio of [Ne II] at 12.81 μm and [Fe II] at 5.34 μm in blue runs along the y-axis and is sensitive to the shock speed, while the ratio of [Fe II] lines at 17.93 and 5.34 μm in green that almost runs parallel to the x-axis is sensitive to the pre-shock density. The dashed green curve is the approximate position of the low-density limit to the [Fe II] flux ratio, below which this ratio is insensitive to pre-shock density. The colored regions represent the de-reddened line ratios from our observations with uncertainties. The colors correspond to those of the apertures in Figure 8. The red half-shaded circle represents aperture 1, where the northern knot is not entirely covered by the MIRI channel 1 field of view (FOV) that has the [Fe II] 5.34 μm line, resulting in overestimated flux ratios.

of $3°.4 \pm 0°.3$. This is similar to the opening angle we measure from the observed jet widths, given the uncertainties. This suggests that the jet is likely ballistically confined, at least within the central 40–1000 au of the driving source; other confinement mechanisms, however, could be at play at larger distances.

The physical conditions of the jet derived from our analysis indicate shock speed of 42–54 km s^{-1} from the base to one end of the jet, suggesting that there is no significant acceleration along the jet. The pre-shock densities estimated are in the range of $\sim$10–2000 cm^{-3}, indicating that the jet is rather tenuous.

The mass-loss rate $\dot{M}_{loss}$ measured from the central protostar as calculated for a suite of jet models and extinction laws is between 0.4 and 1.1 $\times 10^{-10} M_{\odot}$ yr^{-1}. The estimated mass-loss rate is low, even for a very low-mass protostar. The simultaneous accretion rate derived from the OH lines in the MIRI spectrum of IRAS 16253−2429 is $\dot{M}_{acc} = 2.4 \pm 0.8 \times 10^{-9} M_{\odot}$ yr^{-1} (D. Watson et al. 2024, in preparation), commensurate with the low mass-loss rate observed. The protostar appears to be going through a phase of low-mass accretion/ejection currently. It is, however, driving a highly collimated jet, even while in the relatively quiet phase, suggesting that collimated jets are present even when protostars are passing through a low-accretion phase (also see Aso et al. 2023).

Although the protostar IRAS 16253−2429 is currently in a quiescent phase, it must have gone through earlier epochs of high-mass accretion/ejection and is also very likely to go

through active high-accretion phases later in its life, for the following reasons.

The current mass of the central source based on the ALMA observations of the Keplerian disk is about 0.15 $M_{\odot}$ (Aso et al. 2023). At the current mass accretion rate, it would take more than 100 Myr to accrete a mass of 0.15 $M_{\odot}$. IRAS 16253−2429 is a Class 0 protostar, which is likely to be $\ll 1$ Myr old (e.g., Dunham et al. 2014), suggesting that the protostar must have had a period(s) of much higher accretion rate at an earlier stage during which most of the current mass was accreted. Additionally, wide cavities are already present in the envelope of IRAS 16253−2429 (see Federman et al. 2023), which must have been carved out by powerful jets and outflows associated with an earlier high-accretion phase. All these evidences indicate that IRAS 16253−2429 must have been accreting at a significantly higher rate at an earlier time in its life. Zakri et al. (2022) have shown that during these high-accretion phases, a protostar can accrete as much as 100% of its current mass.

The envelope mass of IRAS 16253−2429 estimated from millimeter observations is in the range of 0.2–1 $M_{\odot}$ (Stanke et al. 2006; Enoch et al. 2008; Tobin et al. 2011), depending on the size of the core considered, the opacity values used, and the assumed dust temperature. All measurements and our modeling efforts are consistent with a mass of $\gg 0.2 M_{\odot}$ within an envelope radius of $\sim$4200 au, suggesting that there is significantly more mass in the envelope of IRAS 16253 −2429 than in the central object. If we assume an efficiency of $\sim$30% in converting envelope mass to stellar mass (André et al. 2010; Könyves et al. 2010), then the available mass in the envelope (between 0.2 and 1 $M_{\odot}$) would suggest at least an additional 0.06–0.15 $M_{\odot}$ will be accreted onto the central source. This would make the final mass of IRAS 16253−2429 to be $\sim$0.2–0.3 $M_{\odot}$, which is where the stellar IMF peaks (Bastian et al. 2010).

At the current accretion rate, it would take >50 Myr to accrete this mass, strongly suggesting that the protostar will again go into a high-mass accretion/ejection phase. This is consistent with the results of Zakri et al. (2022), who find that Class 0 protostars undergo bursts every few hundred years that last only a few decades; hence, it is more likely that a protostar is observed in between bursts. In the case of one Class 0 protostar, HOPS 383, the pre- and post-burst periods are characterized by a quiescent state with a very low accretion rate (Zakri et al. 2022). Our JWST observations appear to have captured IRAS 16253−2429 during the interlude between the accretion bursts, i.e., in the quiescent phase, and yet driving a tenuous but highly collimated jet.

The low mass-loss rate that we derive for the protostar is also consistent with the non-detection of a molecular jet from the source. Tabone & Godard (2020) have argued that self-shielding of the jet from FUV photons generated from the central source or from shocks along the jet requires much higher mass-loss rates from the protostar.

5. Summary and Conclusions

We report the discovery of a highly collimated atomic jet as detected in multiple [Fe II] and other FS lines and in H I, originating from the Class 0 protostar IRAS 16253−2429 in the Ophiuchus molecular cloud (140 pc), the least luminous source in the IPA program. No collimated molecular jet is detected in CO, SiO, in the (sub)millimeter with ALMA or H$_2$

in the IR with JWST. We determine the following properties for the jets/outflows from IRAS 16253-2429:

1. The jet (as seen in the [Fe II] line at 5.34 μm) is 23 ± 4 au wide at the base with an opening angle of $2°6 \pm 0°5$.
2. The jet seen in [Fe II] lines has a velocity of 169 ± 15 km s^{-1} after correcting for inclination. The jets on either side of the protostar appear to have similar velocities that remain almost constant as a function of distance from the center.
3. The jet is about 445 au long (after correcting for inclination) on either side with a dynamical timescale of $\sim$12.5 yr.
4. We determine the line-of-sight extinction A_V along the jet using H$_2$ lines in the cavity, which gives A_V values ranging from 12.3 to 26.6 mag.
5. Using the extinction-corrected flux ratios of [Ne II] at 12.81 μm and the [Fe II] lines at 5.34 μm and 17.936 μm, we derive a shock speed of 54 km s^{-1} and a pre-shock density of 2.0×10^3 cm^{-3} at the base of the jet.
6. Assuming a cylindrical jet with a cross-sectional width of 23 au and using the jet velocity of 169 km s^{-1} along with the derived pre-shock density and shock speed, we compute the mass-loss rate from the jet to be 0.4–$1.1 \times 10^{-10} M_\odot$ yr^{-1}.

The low mass-loss rate derived is consistent with the simultaneous measurements of low accretion rate of $\sim$2.4 $\times$ $10^{-9} M_\odot$ yr^{-1} for IRAS 16253$-$2429 (D. Watson et al. 2024, in preparation), indicating that the protostar is likely in the quiescent accretion phase. Our results show that even a very low-mass protostar in a quiescent phase with low accretion rate can still drive a highly collimated jet.

Acknowledgments

Data Availability

All of the data presented in this article were obtained from the Mikulski Archive for Space Telescopes (MAST) at the Space Telescope Science Institute. The specific observations analyzed can be accessed via doi:10.17909/3kky-t040.

Appendix

Figure 11 shows the H$_2$ rotation diagrams for all apertures. The rotation temperature and A_V values for different apertures are listed in Table (currently 4 after suggested changes 2).
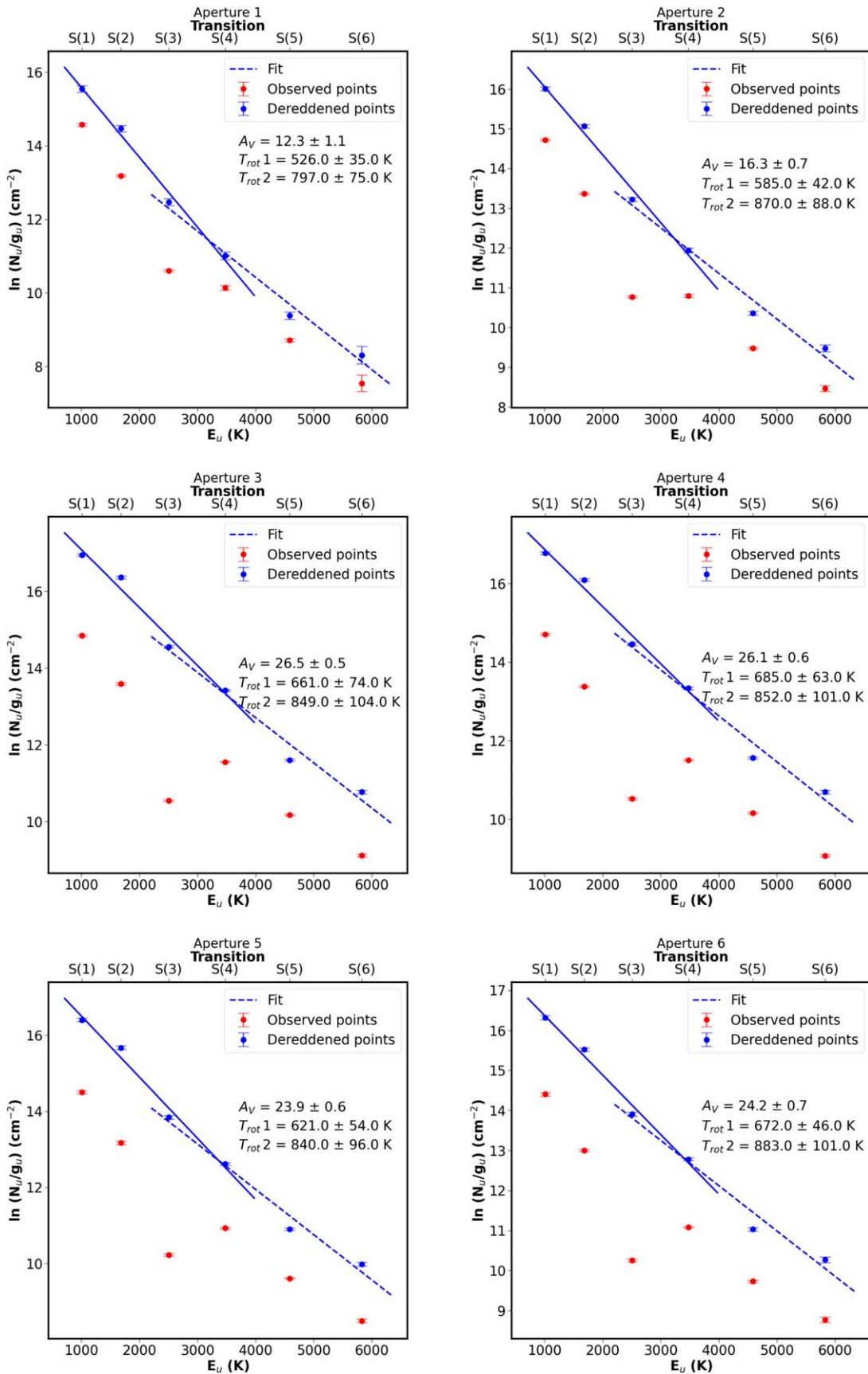
Figure 11. The H_2 rotation diagram for all apertures shown in Figure 8. Also shown are the observed points (red), the de-reddened points (blue), as well as the fit to them. The extinction value A_V as well as the rotation temperatures are listed in the figure. The y-error bars on the observed (red) points are computed based on the uncertainties in the integrated flux determined by a Gaussian fit to the lines using the measured uncertainties from the IFU error cubes. The y-error bars on the de-reddened (blue) points also incorporate the error in A_V from the fit.

Narang et al.

ORCID iDs

Mayank Narang ⬤ https://orcid.org/0000-0002-0554-1151
P. Manoj ⬤ https://orcid.org/0000-0002-3530-304X
Himanshu Tyagi ⬤ https://orcid.org/0000-0002-9497-8856
Dan M. Watson ⬤ https://orcid.org/0000-0001-8302-0530
S. Thomas Megeath ⬤ https://orcid.org/0000-0001-7629-3573
Samuel Federman ⬤ https://orcid.org/0000-0002-6136-5578
Adam E. Rubinstein ⬤ https://orcid.org/0000-0001-8790-9484
Robert Gutermuth ⬤ https://orcid.org/0000-0002-6447-899X
Alessio Caratti o Garatti ⬤ https://orcid.org/0000-0001-8876-6614
Henrik Beuther ⬤ https://orcid.org/0000-0002-1700-090X
Tyler L. Bourke ⬤ https://orcid.org/0000-0001-7491-0048
Ewine F. Van Dishoeck ⬤ https://orcid.org/0000-0001-7591-1907
Neal J. Evans, II ⬤ https://orcid.org/0000-0001-5175-1777
Guillem Anglada ⬤ https://orcid.org/0000-0002-7506-5429
Mayra Osorio ⬤ https://orcid.org/0000-0002-6737-5267
Thomas Stanke ⬤ https://orcid.org/0000-0002-5812-9232
James Muzerolle ⬤ https://orcid.org/0000-0002-5943-1222
Leslie W. Looney ⬤ https://orcid.org/0000-0002-4540-6587
Yao-Lun Yang ⬤ https://orcid.org/0000-0001-8227-2816
Pamela Klaassen ⬤ https://orcid.org/0000-0001-9443-0463
Nicole Karnath ⬤ https://orcid.org/0000-0003-3682-854X
Prabhani Atnagulov ⬤ https://orcid.org/0000-0002-4026-126X
Nashanty Brunken ⬤ https://orcid.org/0000-0001-7826-7934
William J. Fischer ⬤ https://orcid.org/0000-0002-3747-2496
Elise Furlan ⬤ https://orcid.org/0000-0001-9800-6248
Joel Green ⬤ https://orcid.org/0000-0003-1665-5709
Nolan Habel ⬤ https://orcid.org/0000-0002-2667-1676
Lee Hartmann ⬤ https://orcid.org/0000-0003-1430-8519
Hendrik Linz ⬤ https://orcid.org/0000-0002-8115-8437
Pooneh Nazari ⬤ https://orcid.org/0000-0002-4448-3871
Riwaj Pokhrel ⬤ https://orcid.org/0000-0002-0557-7349
Rohan Rahatgaonkar ⬤ https://orcid.org/0000-0002-5350-0282
Will R. M. Rocha ⬤ https://orcid.org/0000-0001-6144-4113
Patrick Sheehan ⬤ https://orcid.org/0000-0002-9209-8708
Katerina Slavicinska ⬤ https://orcid.org/0000-0002-7433-1035
Amelia M. Stutz ⬤ https://orcid.org/0000-0003-2300-8200
John J. Tobin ⬤ https://orcid.org/0000-0002-6195-0152
Lukasz Tychoniec ⬤ https://orcid.org/0000-0002-9470-2358
Scott Wolk ⬤ https://orcid.org/0000-0002-0826-9261

References

André, P., Men'shchikov, A., Bontemps, S., et al. 2010, A&A, 518, L102
Agra-Amboage, V., Cabrit, S., Dougados, C., et al. 2014, A&A, 564, A11
Appel, S. M., Burkhart, B., Semenov, V. A., et al. 2023, ApJ, 954, 93
Argyriou, I., Glasse, A., Law, D. R., et al. 2023, A&A, 675, A111
Aso, Y., Kwon, W., Ohashi, N., et al. 2023, ApJ, 954, 101
Asplund, M., Grevesse, N., Sauval, A. J., et al. 2009, ARA&A, 47, 481
Bally, J. 2016, ARA&A, 54, 491
Barsony, M., Wolf-Chase, G. A., Ciardi, D. R., et al. 2010, ApJ, 720, 64
Bastian, N., Covey, K. R., & Meyer, M. R. 2010, ARA&A, 48, 339
Beuther, H., van Dishoeck, E. F., Tychoniec, L., et al. 2023, A&A, 673, A121
Blandford, R. D., & Payne, D. G. 1982, MNRAS, 199, 883
Böker, T., Arribas, S., Lützgendorf, N., et al. 2022, A&A, 661, A82
Caratti o Garatti, A., Giannini, T., Nisini, B., et al. 2006, A&A, 449, 1077
Chapman, N. L., Mundy, L. G., Lai, S.-P., et al. 2009, ApJ, 690, 496
Del Zanna, G., Dere, K. P., Young, P. R., & Landi, E. 2021, ApJ, 909, 38D
Dunham, M. M., Stutz, A. M., Allen, L. E., et al. 2014, in Protostars and
    Planets VI, ed. H. Beuther et al., 195
Enoch, M. L., Evans, N. J., Sargent, A. I., et al. 2008, ApJ, 684, 1240
Fall, S. M., Krumholz, M. R., & Matzner, C. D. 2010, ApJL, 710, L142

Federman, S., Megeath, S. T., Rubinstein, A. E., et al. 2023a, arXiv:2310.03803
Federman, S., Megeath, S. T., Tobin, J. J., et al. 2023b, ApJ, 944, 49
Federrath, C. 2015, MNRAS, 450, 4035
Fischer, W. J., Megeath, S. T., Furlan, E., et al. 2017, ApJ, 840, 69
Frank, A., Ray, T. P., Cabrit, S., et al. 2014, in Protostars and Planets VI, ed.
    H. Beuther et al. (Tucson, AZ: Univ. Arizona Press), 451
Gordon, I. E., Rothman, L. S., Hargreaves, R. J., et al. 2022, JQSRT, 277, 107949
Guszejnov, D., Grudić, M. Y., Offner, S. S. R., et al. 2022, MNRAS, 515, 4929
Habel, N. M., Megeath, S. T., Booker, J. J., et al. 2021, ApJ, 911, 153
Harsono, D., Bjerkeli, P., Ramsey, J. P., et al. 2023, ApJL, 951, L32
Hartmann, L., Herczeg, G., & Calvet, N. 2016, ARA&A, 54, 135
Hensley, B. S., & Draine, B. T. 2021, ApJ, 906, 73
Hsieh, C.-H., Arce, H. G., Li, Z.-Y., et al. 2023, ApJ, 947, 25
Hsieh, T.-H., Hirano, N., Belloche, A., et al. 2019, ApJ, 871, 100
Jakobsen, P., Ferruit, P., Alves de Oliveira, C., et al. 2022, A&A, 661, A80
Jones, O. C., Álvarez-Márquez, J., Sloan, G. C., et al. 2023, MNRAS, 523, 2519
Khanzadyan, T., Gredel, R., Smith, M. D., et al. 2004, A&A, 426, 171
Könyves, V., André, P., Men'shchikov, A., et al. 2010, A&A, 518, L106
Koo, B.-C., Raymond, J. C., & Kim, H.-J. 2016, JKAS, 49, 109
Kramida, A., Ralchenko, Yu., Reader, J. & and NIST ASD Team 2023, NIST
    Atomic Spectra Database, ver. 5.11, https://physics.nist.gov/asd, doi:10.18434/T4W30F
Law, D. D., Morrison, J. E., Argyriou, I., et al. 2023, AJ, 166, 45
Lebreuilly, U., Hennebelle, P., Maury, A., et al. 2023, arXiv:2309.05397
Manoj, P., Watson, D. M., Neufeld, D. A., et al. 2013, ApJ, 763, 83
Maret, S., Bergin, E. A., Neufeld, D. A., et al. 2009, ApJ, 698, 1244
Matt, S., & Pudritz, R. E. 2005, ApJL, 632, L135
Matt, S., & Pudritz, R. E. 2008, ApJ, 678, 1109
McClure, M. 2009, ApJL, 693, L81
Megeath, T., Anglada, G., Atnagulov, P., et al. 2021, JWST Proposal. Cycle 1,
    ID. #1802
Najita, J. R., & Shu, F. H. 1994, ApJ, 429, 808
Narang, M., Puravankara, M., Tyagi, H., et al. 2023, JApA, 44, 92
Nazari, P, Rocha, W. R. M., Rubinstein, A. E., et al. 2024, arXiv:2401.07901
Neufeld, D. A., Nisini, B., Giannini, T., et al. 2009, ApJ, 706, 170
Pelletier, G., & Pudritz, R. E. 1992, ApJ, 394, 117
Podio, L., Tabone, B., Codella, C., et al. 2021, A&A, 648, A45
Pokhrel, R., Gutermuth, R. A., Krumholz, M. R., et al. 2021, ApJL, 912, L19
Pokhrel, R., Megeath, S. T., Gutermuth, R. A., et al. 2023, ApJS, 266, 32
Pudritz, R. E., & Norman, C. A. 1983, ApJ, 274, 677
Pudritz, R. E., Ouyed, R., Fendt, C., et al. 2007, in Protostars and Planets V, ed.
    V. B. Reipurth, D. Jewitt, & K. Keil (Tucson, AZ: Univ. Arizona
    Press), 277
Raga, A. C., Canto, J., Binette, L., et al. 1990, ApJ, 364, 601
Raga, A. C., & Kofman, L. 1992, ApJ, 386, 222
Ray, T. P., & Ferreira, J. 2021, NewAR, 93, 101615
Ray, T. P., McCaughrean, M. J., Caratti o Garatti, A., et al. 2023, Natur, 622, 48
Reipurth, B., Davis, C. J., Bally, J., et al. 2019, AJ, 158, 107
Rieke, G. H., Wright, G. S., Böker, T., et al. 2015, PASP, 127, 584
Rubinstein, A. E., Karnath, N., Quillen, A. C., et al. 2023, ApJ, 948, 39
Rubinstein, A. E., Tyagi, H., Nazari, P., et al. 2023, arXiv:2312.07807
Shang, H., Li, Z.-Y., & Hirano, N. 2007, in Protostars and Planets V, ed.
    V. B. Reipurth, D. Jewitt, & K. Keil (Tucson, AZ: Univ. of Arizona
    Press), 261
Shu, F., Najita, J., Ostriker, E., et al. 1994, ApJ, 429, 781
Spruit, H. C. 1996, Evolutionary Processes in Binary Stars, Vol. 477
    (Dordrecht: Kluwer), 249
Stanke, T., Smith, M. D., Gredel, R., et al. 2006, A&A, 447, 609
Sutherland, R., Dopita, M., Binette, L., et al., 2018 MAPPINGS V:
    Astrophysical plasma modeling code, Astrophysics Source Code Library,
    ascl:1807.005
Tabone, B., Godard, B., Pineau des Forêts, G., et al. 2020, A&A, 636, A60
Tayal, S. S., & Zatsarinny, O. 2018, PhRvA, 98, 012706
Tobin, J. J., Hartmann, L., Chiang, H.-F., et al. 2011, ApJ, 740, 45
Wardle, M., & Koenigl, A. 1993, ApJ, 410, 218
Watson, D. M., Calvet, N. P., Fischer, W. J., et al. 2016, ApJ, 828, 52
Wright, G. S., Wright, D., Goodson, G. B., et al. 2015, PASP, 127, 595
Yang, Y.-L., Green, J. D., Pontoppidan, K. M., et al. 2022, ApJL, 941, L13
Yen, H.-W., Koch, P. M., Takakuwa, S., et al. 2017, ApJ, 834, 178
Zakri, W., Megeath, S. T., Fischer, W. J., et al. 2022, ApJL, 924, L23
Zucker, C., Speagle, J. S., Schlafly, E. F., et al. 2020, A&A, 633, A51